Spatiotemporal Correlation Analysis of Noise-Derived Seismic Body Waves With Ocean Wave Climate and Microseism Sources

Lei Li[1,2] (iD), Pierre Boué[2] (iD), Lise Retailleau[3,4] (iD), and Michel Campillo[2] (iD)

[1]State Key Laboratory of Earthquake Dynamics, Institute of Geology, CEA, Beijing, China, [2]Université Grenoble Alpes, Université Savoie Mont Blanc, CNRS, IRD, IFSTTAR, ISTerre, Grenoble, France, [3]Université de Paris, Institut de physique du globe de Paris, CNRS, Paris, France, [4]Observatoire Volcanologique du Piton de la Fournaise, Institut de physique du globe de Paris, La Plaine des Cafres, France

Abstract Seismic signals can be extracted from ambient noise wavefields by the correlation technique. Recently, a prominent *P*-type phase was observed from teleseismic noise correlations in the secondary microseism period band. The phase is named P_{dmc} in this paper, corresponding to its origin from the interference between the direct *P* waves transmitting through the deep mantle and the core (*P* and *PKPab* waves). We extract the phase by correlating noise records from two seismic networks in the Northern Hemisphere and locate the microseism sources that are efficient for the P_{dmc} construction in the South Pacific. We investigate the spatiotemporal links of the P_{dmc} signal with global oceanic waves and microseism sources. Interestingly, the correlation with wave height is higher in several regions surrounding the effective source region, rather than in the effective source region. The P_{dmc} amplitude is highly correlated with the power of the effective microseism sources. Also, it is apparently correlated with ineffective sources in the Southern Hemisphere and anticorrelated with sources in the Northern Hemisphere. We ascribe the correlation with the ineffective southern sources to the spatiotemporal interconnections of the southern sources. The anticorrelation with northern sources can be explained by the reverse seasonal patterns between the southern and northern sources and by that the northern sources impede the signal construction. The signal construction from noise correlations relies on the competition between the effective and ineffective sources, not just on the power of the effective sources. This principle should be valid in a general sense for noise-derived signals.

Plain Language Summary Earth is experiencing tiny but incessant movement induced by natural forces, particularly, storm-driven ocean waves. While this ambient seismic noise (microseism) was deemed a nuisance in the past, it can be turned into signals via the seismic correlation technique. Recently, a new *P*-type phase was derived from the noise correlations between two regional seismic networks. The noise-derived phase originates from the correlation between *P* waves that propagate through the deep mantle and outer core of the Earth. The temporal amplitude variations of the noise-derived signals are compared with the variations of microseism sources in the oceans. We show that the signal emergence depends on the competition between the sources in a specific region that contribute to the signals and sources in other regions. The conclusion can be generalized to other noise-derived seismic phases. We also analyze the links of the noise-derived signals to ocean waves. In our case, the ocean waves in the contributing source region are dominated by wind seas forced by local winds, whereas the excitation of microseisms is primarily owing to the freely traveling swells generated by oceanic storms in surrounding regions.

1. Introduction

The incessant background vibrations of Earth had been observed as early as the birth of seismometers in the later nineteenth century (Bernard, 1990; Dewey & Byerly, 1969; Ebeling, 2012). They were termed "microseisms" due to their tiny amplitudes. With more apparatus deployed worldwide, it was soon recognized that microseisms are ubiquitous and irrelevant to seismicity. The observation of microseisms aroused interests from various disciplines. Researchers linked the generation of microseisms to atmosphere processes and ocean wave activity. Meteorologists tried to employ land observations of microseisms to track remote oceanic storms (e.g., Harrison, 1924). Since the midtwentieth century, it has been well known that microseisms

are excited by storm-driven ocean waves. The most energetic microseisms that dominate the seismic noise spectra, namely, the so-called secondary microseisms at seismic periods around 7 s (Peterson, 1993), are excited by the nonlinear interactions between nearly equal-frequency ocean waves propagating in nearly opposite directions (Hasselmann, 1963; Longuet-Higgins, 1950). The periods of the excited secondary microseisms are half those of the colliding ocean waves. The excitation source is equivalent to a vertical pressure applied to the water surface, which is proportional to the product of the heights of the opposing equal-frequency waves. Due to this second-order relation, moderate sea states can sometimes generate loud microseism noise (Obrebski et al., 2012). Thus, the presence of a strong microseism event does not necessarily imply a locally intense sea state.

By coupling the excitation theory of secondary microseisms proposed by Longuet-Higgins (1950) with the ocean wave action model, Kedar et al. (2008) modeled the secondary microseism excitations in the North Atlantic and validated the numerical modeling by comparing with inland seismological observations. Afterward, more authors simulated the oceanic microseism sources, and some reported the consistency between predictions and observations (e.g., Ardhuin et al., 2011, 2015; Hillers et al., 2012; Nishida & Takagi, 2016; Stutzmann et al., 2012). Stopa et al. (2019) compared the microseism simulations with real observations to validate their corrections to the global reanalysis wind fields, which systematically reduced the residuals in the wave hindcast over the past decades.

The seismic excitation by an oceanic microseism source is essentially akin to that by an earthquake, in that the seismic wavefield recorded at any point is a convolution of the source time function with the Green function of the propagating medium between source and receiver. Their main difference lies in the source process. For earthquakes, the sudden rupture of faults leads to short-duration, impulsive source time functions. Isolated seismic phases are generally distinguishable from the seismograms. In contrast, the excitation of microseisms, approximated as Gaussian random process by some authors (Peterson, 1993; Steim, 2015), is incessant, leading to long, random-like source time functions. The convolution mixture signals are not directly discernible from the seismograms. With array beamforming (Rost & Thomas, 2002) or correlation technique (Campillo & Paul, 2003; Shapiro & Campillo, 2004), specific phases from distant microseism sources have been identified from microseism noise records (e.g., Euler et al., 2014; Gal et al., 2015; Gerstoft et al., 2008; Landès et al., 2010; Liu et al., 2016; Meschede et al., 2017, 2018; Nishida & Takagi, 2016; Reading et al., 2014; Retailleau & Gualtieri, 2019; Zhang et al., 2010). The correlation technique is advantageous in that, by correlating the noise records at two receivers, explicit seismic signals can be derived. Noise-derived surface waves have been used to infer the azimuthal and seasonal changes of noise sources (e.g., Stehly et al., 2006). Noise-derived body waves can provide better constrains in imaging the noise sources (Landès et al., 2010). Recently, deep body waves that propagate through the mantle and core have been extracted from ambient noise (e.g., Boué et al., 2013; Lin et al., 2013; Nishida, 2013; Poli et al., 2015; Retailleau et al., 2020; Spica et al., 2017; Xia et al., 2016). The noise-derived body waves are valuable for surveying the deep structure and for understanding the links between seismological observations and atmospheric/oceanographic phenomena.

Hillers et al. (2012) made the first global-scale comparison between the oceanic microseism sources derived from seismological observations and oceanographic modeling. The seismologically derived data (time resolution: 13 days; spatial resolution: 2.5° latitude × 5° longitude) are the global backprojections of near-zero lag P signals generated from the cross correlations of microseism P waves at seismic array (Landès et al., 2010). The modeled data (time resolution: 3 hr; spatial resolution: 1° latitude × 1.25° longitude) are a global extension of the numerical simulation by Kedar et al. (2008). The two data sets are resampled to common resolutions for comparison. For the seismologically derived data, the backprojection is based on the relationship between the source-receiver distance and the horizontal slowness of teleseismic P wave. However, seismic phases that have common slownesses (e.g., P and PP waves) cannot be discriminated in this method (Gerstoft et al., 2008; Landès et al., 2010). Thus, the imaged sources are somewhat ambiguous. For the modeled data, coastal reflections of ocean waves, which can play a role in the ocean wave-wave interactions at near-coast regions (Ardhuin et al., 2011; Longuet-Higgins, 1950), are neglected. Due to the resonance of seismic waves in the water columns, bathymetry can have significant effect on the excitation of microseisms (Hillers et al., 2012; Kedar et al., 2008; Longuet-Higgins, 1950). The importance to account for the bathymetric effect on the microseism P wave excitations has been addressed in several studies (e.g., Euler

et al., 2014; Gal et al., 2015; Meschede et al., 2017). Hillers et al. (2012) considered the bathymetric effect but using the amplification factors derived by Longuet-Higgins (1950) for surface waves.

Rascle and Ardhuin (2013) established an oceanographic hindcast database that includes global oceanic secondary microseism sources of a 3-hr time resolution and a 0.5° spatial resolution. Coastal reflections were accounted for in the modeling (Ardhuin et al., 2011). Regarding the bathymetric effect on microseism excitations, Gualtieri et al. (2014) proposed the formulae for body waves based on ray theory. Concerning the localization of noise sources, Li et al. (2020) developed a double-array method that can estimate the respective slownesses of the interfering waves and, thereby, provide better constrains for the determination of the correlated seismic phases. The microseism sources that are effective for the derivation of seismic signals from noise records can be mapped by backprojecting the noise-derived signals along the ray paths of the correlated phases. The double-array configuration eliminates the ambiguity in determining the effective source region (Fresnel zone). In this study, we integrate these new progresses to survey the associations of noise-derived body waves to ocean wave activity and microseism excitations.

This paper is organized as follows. In section 2, we review the main results of Li et al. (2020) who reported the observation of a prominent *P*-type phase from the noise correlations between two regional seismic networks at teleseismic distance. The noise-derived phase has its spectral content concentrated in the period band of the secondary microseisms that are excited by the nonlinear ocean wave-wave interactions. In this paper, we denote the phase as P_{dmc}, corresponding to the fact that the phase originates from the correlation between the sirect *P* waves that transmit through the deep mantle and the outer core (microseism *P* and *PKPab* waves). In section 3, we estimate the temporal variations in the P_{dmc} amplitude and refute the associations to seismicity. In section 4, correlation analysis is used to unveil the spatiotemporal links of the P_{dmc} signal with the global oceanic wave climate and microseism sources. Last, we discuss the significance of this study in seismology, oceanography, and climate science.

2. Noise-Derived P_{dmc} Phase

Li et al. (2020) correlated the seismic noise records from two regional seismic networks at teleseismic distance: the FNET array in Japan and the LAPNET array in Finland (Figure 1a). The continuous seismograms were divided into 4 hr segments and whitened in the frequency domain. Segments with large spikes (like earthquakes) were discarded. The available segments of each FNET-LAPNET station pairs were correlated. For more technical details, see section 2 of Li et al. (2020). From the vertical-vertical components of the FNET-LAPNET noise correlations, they observed coherent spurious arrivals (the P_{dmc} phase named in the previous section) that emerged ~200 s earlier than the direct *P* waves (Figure 1b). By estimating the respective slownesses of the interfering waves and their time delay, it is unveiled that a quasi-stationary phase interference between the teleseismic *P* waves at FNET and the *PKPab* waves at LAPNET, emanating from noise sources in the ocean south of New Zealand (NZ), leads to the noise-derived P_{dmc} phase (Figure 1c). The quasi-stationary phase condition refers to that the interfering waves have no common path or common slowness, but the stack of correlation functions over a range of sources can still be constructive as an effect of finite frequency. This observation contrasts with the strict stationary phase condition that has been employed by Phạm et al. (2018) to explain the spurious body phases in the earthquake coda correlations. The strict condition implies the existence of sources in the stationary-phase region, or say, the correlated waves have common ray paths or common slownesses. Li et al. (2020) substantiates the explanation of quasi-stationary phase for the observed P_{dmc} signals with numerical experiments based on ray theory and based on spectral-element modeling and highlighted the discrepancies between (microseism) noise correlations and coda correlations.

The P_{dmc} phase has an apparent slowness of 4.6 s/degree, while the slownesses of the interfering *P* and *PKPab* waves are 4.7 and 4.2 s/degree, respectively. The dominant period of the P_{dmc} phase is 6.2 s, typical for secondary microseisms. The observation of the P_{dmc} phase is time asymmetric (supporting information Figure S1a). Its absence from the mirror side is ascribed to the faintness of the corresponding source in the low-latitude Atlantic (Figure S1b).

There are several advantages to investigating the links between noise-derived signals and microseism sources with the P_{dmc} phase. First, the correlated *P* and *PKPab* waves are both prominent phases in the
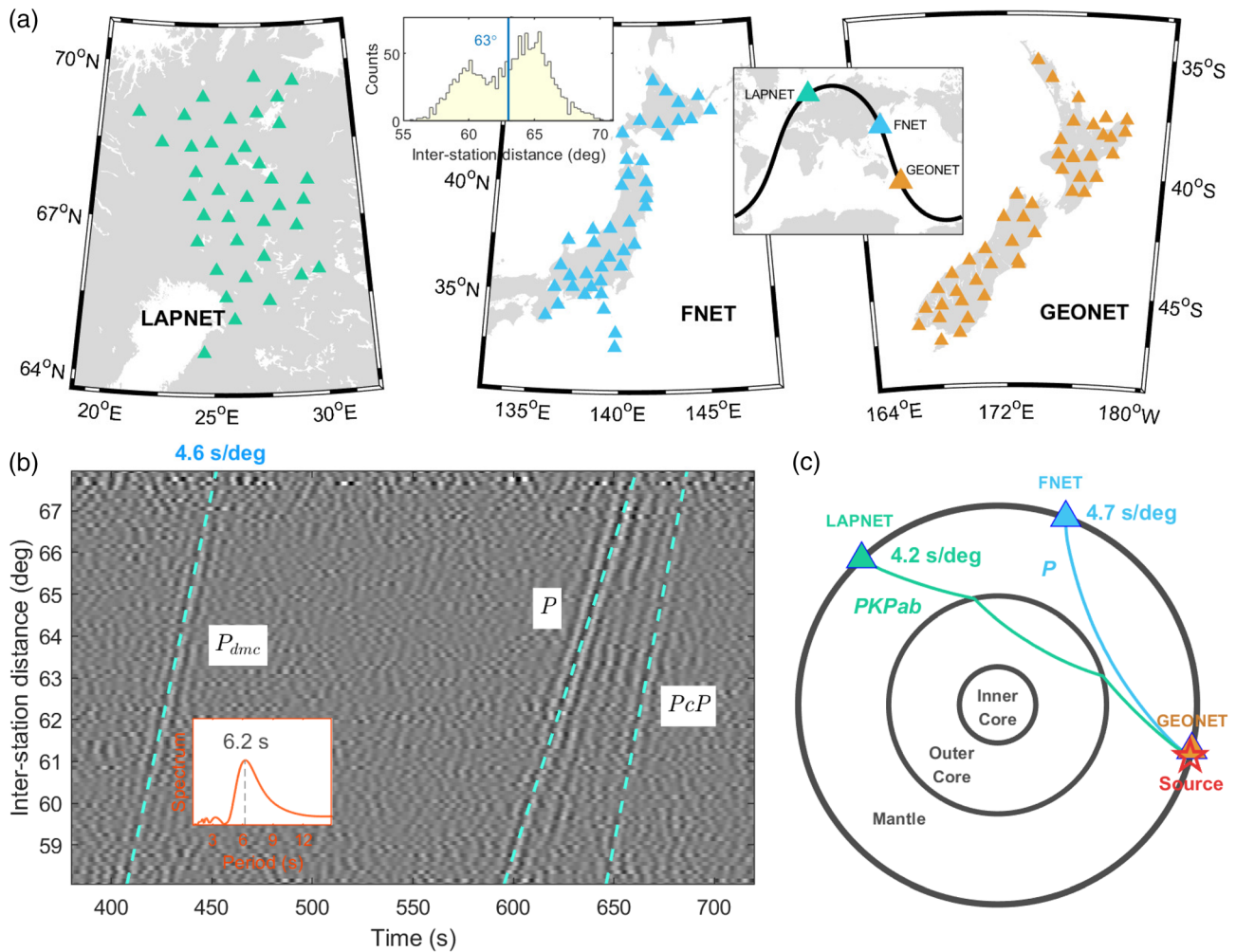
Figure 1. (a) Three regional broadband seismic networks used in this study: (left) the LAPNET array in Finland (38 stations); (center) the FNET array in Japan (41 stations); (right) the GEONET array in New Zealand (46 stations). The histogram inset shows the distribution of the separation distances between the 1,558 FNET-LAPNET station pairs. The center-to-center distance is 63° between LAPNET and FNET and 85° between FNET and GEONET. The global inset shows the geographical locations of the three networks that are aligned on a great circle (dark line). (b) Annual FNET-LAPNET noise correlations that are filtered between 5 and 10 s and stacked over time and in 0.1° interstation distance bins. The spectrum inset indicates that the P_{dmc} phase has a 6.2 s peak period. (c) Ray paths of the interfering waves that generate the P_{dmc} phase. The effective source region is close to GEONET.

ballistic microseism wavefields. The P_{dmc} phase is easily observable from noise correlations, even between some single station pairs and on some single days (Figure S2). Second, the isolation of P_{dmc} signals avoids potential bias caused by other prominent signals. Third, the effective sources are confined in a limited, unique region (Fresnel zone). In contrast, noise-derived surface waves have a broad Fresnel zone around the line across the correlated stations, and noise-derived P waves can have multiple Fresnel zones (see Figure 5 of Boué et al., 2014, for instance). The uniqueness of the effective source region can facilitate the study on the correlation between the noise-derived signals and the effective sources. Fourth, the correlated FNET and LAPNET networks are next to the northern Pacific and Atlantic, respectively, while the effective source region locates in the southern Pacific. The northern oceans have consistent seasonal variation pattern distinct from (reverse to) that of the southern oceans (Hillers et al., 2012; Landès et al., 2010; Reading et al., 2014; Stehly et al., 2006; Stutzmann et al., 2009; Turner et al., 2020). These geographical configurations make the observations easier to interpret. Last, there happens to be a seismic array (GEONET) in NZ next to the effective source region for the P_{dmc} phase. The seismic data from GEONET provide extra support to our study.

3. Temporal Variations

We extract the temporal variations of the P_{dmc} signals by beamforming the FNET-LAPNET noise correlations on a daily basis. The daily noise correlations are shifted and stacked by

$$B(t) = \left\langle C_{ij}\left(t + \left(d_{ij} - d_0\right) \cdot p\right)\right\rangle, \tag{1}$$

with $\langle\cdot\rangle$ the mean operator, C_{ij} and d_{ij} the correlation function and the distance between the ith FNET station and the jth LAPNET station, d_0 the reference distance (63°), p the apparent slowness of the P_{dmc} phase (4.6 s/degree), and t the time. The image in Figure 2 shows the envelopes of the daily beams computed from the Hilbert transform of Equation 1, with the daily P_{dmc} strength by averaging the envelope amplitudes plotted in the top panel. The strength of daily P_{dmc} signals varies strikingly, extremely strong on some single days (e.g., see the labeled dates in the P_{dmc} strength curve) but indiscernible on most other days.

Considering that the region of effective source is tectonically active, one should investigate the plausible connection between the P_{dmc} signals and seismicity. From Figure 2, it is obvious that P_{dmc} is decorrelated with the NZ seismicity. Also, it shows no connection with global large earthquakes as has been observed for coda-derived core phases at periods of 20 to 50 s (Boué et al., 2014; Lin & Tsai, 2013). That again demonstrates the substantial difference between ambient noise correlations and earthquake coda correlations, as emphasized by Li et al. (2020). The P_{dmc} strength exhibits an obvious pattern of seasonal variation. The seasonal pattern does not favor a tectonic origin because of the lack of a seasonal pattern in seismicity. Instead, an oceanic origin is more favored because of the well-documented fact that oceanic wave activity and microseism excitations show similar seasonal pattern: more powerful during the local winter (e.g., Hillers et al., 2012; Landès et al., 2010; Reading et al., 2014; Stehly et al., 2006; Stutzmann et al., 2009). Next, we analyze the correlations between P_{dmc} signals and oceanographic data at a global scale.

4. Correlation Analysis

The sea state is composed of ocean waves at various frequencies and propagation directions. The nonlinear interaction between nearly equal-frequency ocean waves traveling in nearly opposite directions is equivalent to a vertical random pressure applied to the ocean surface (Hasselmann, 1963; Longuet-Higgins, 1950), so that microseisms are generated. Figure 3a shows a global map of average power spectral density (PSD) of the equivalent surface pressure for a seismic period of 6.2 s, during the northern winter months of 2008. The hindcast PSD data are simulated by Ardhuin et al. (2011) and Rascle and Ardhuin (2013), based on the microseism excitation theory of Longuet-Higgins (1950) and Hasselmann (1963). The most energetic microseism excitations occur in the northern Atlantic south of Greenland and Iceland (near LAPNET) and in the northern Pacific between Japan and Alaska (near FNET). Figure 3b shows the map for the austral winter months, with the strongest excitations occurring between NZ and Antarctic (near GEONET). The seasonal pattern of oceanic microseism excitations results from the same pattern of global wave climate (Figures 3e and 3f). The seasonal pattern of the P_{dmc} strength agrees with that of the microseism excitation and wave climate in the effective source region south of NZ.

We compute the correlation coefficient (denoted as r) between the P_{dmc} strength and the source PSDs at each grid point and thereby obtain a global correlation map (Figure 3c). The largest r value for P_{dmc} and source PSD arises at [47°S, 177°E] in the effective source region (E in Figure 3c). The corresponding time series of daily source PSDs is plotted in Figure 4, in parallel with the P_{dmc} strength. Large peaks in the P_{dmc} series have good correspondence with large peaks in the source PSD series. From Figure 3c, one can observe a broad region of positive r values (red colors; roughly, South Atlantic, South Pacific, and Indian Ocean). However, the positive correlation does not imply a causality between the P_{dmc} phase and the sources outside the effective region E. We ascribe the apparent positive correlation to the spatial correlation of the time-varying microseism excitation. As shown in Figure 3d, the source at [47°S, 177°E] in region E exhibits a similar pattern of apparent correlations with global sources as in Figure 3c. Despite the fact that the microseism excitations at varying locations are independent (Hasselmann, 1963), we note that the independence refers only to the phase information. The time variations of microseism source power are spatially associated. That is not surprising since the interacting ocean waves that excite microseisms could be driven by the same storms, and swells can propagate freely over thousands of kilometers away (Ardhuin
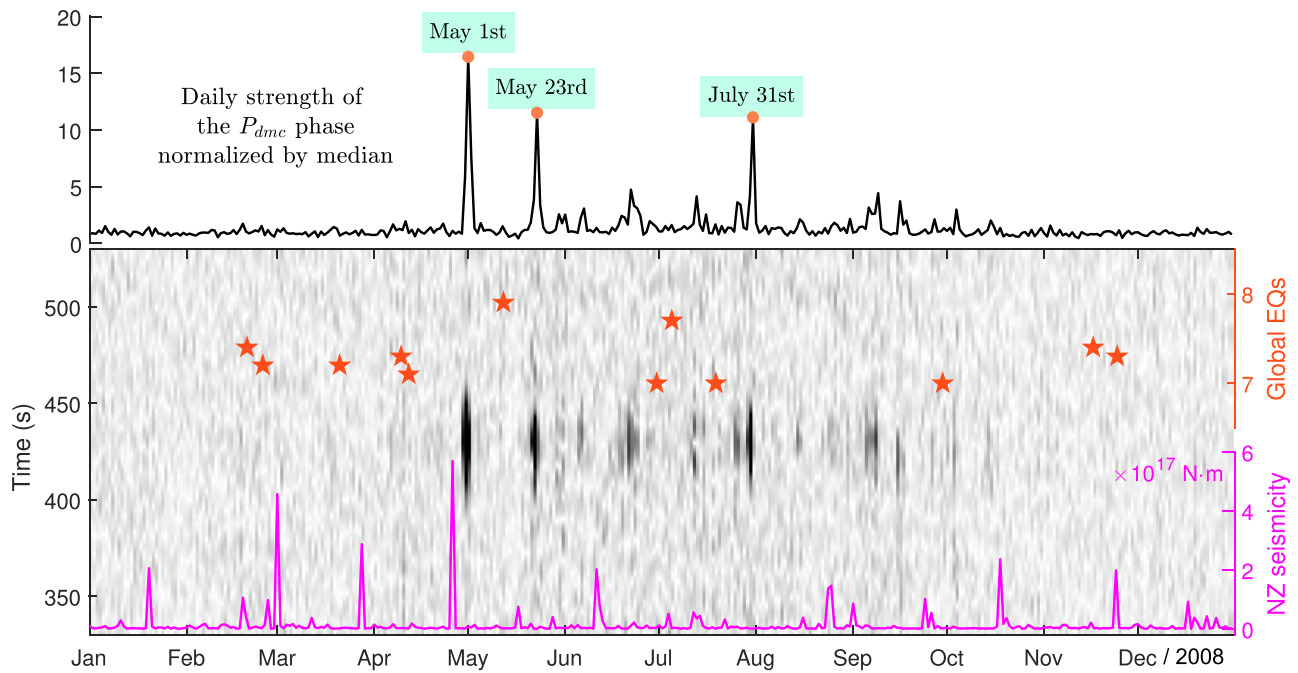
Figure 2. Temporal variations in the strength of daily P_{dmc} signals, in comparison with the daily cumulative seismic moments in NZ (pink line at bottom; for earthquake magnitudes above 2.0 in GEONET catalog) and global large earthquakes (stars; magnitudes above 7.0 in USGS catalog; see Table S1 for a full list of earthquakes in 2008 above magnitude 5.5). The background image is composed of columns of daily envelopes of beamed FNET-LAPNET noise correlations. Darker color represents larger amplitude. The curve on the top shows the daily P_{dmc} strength derived from the daily envelopes. Dates of the three largest peaks are labeled.

et al., 2009). We also notice there are high-r regions that may not be fully explained by the spatial association. These regions are characterized by low intensity of microseism excitations in Figures 3a and 3b. A striking example is around [12°N, 88°E] in the Bay of Bengal (F in Figure 3c). From Figure 4, it can be seen that the source PSD series for [12°N, 88°E] is dominated by a single peak around 1 May, coincident with the largest P_{dmc} peak. This coincidence leads to a high value of correlation coefficient. However, the Bay of Bengal is far away from the FNET-LAPNET great circle, which is inconsistent with the source imaging shown later in Figure 5. Thus, the high correlation is spurious and does not imply a causality relationship between the microseism sources in the Bay of Bengal and the P_{dmc} signals. Figures 3g and 3h show the correlation maps for h_s, which will be discussed later.

As shown in Figure 4, prominent peaks in the P_{dmc} series have correspondence in the source PSD series for the effective source at [47°S, 177°E]. However, there are some peaks in the latter without correspondence in the former (e.g., see the labeled dates in Figure 4b). Note that here the P_{dmc} strength is compared to the microseism source PSD at single point in Figure 4, whereas the effective sources spread over a region. One needs to verify if the peak disparities observed from Figures 4a and 4b can be ascribed to the neglect of the spreading of the effective source region. To evaluate an overall microseism excitation in the effective source region, the bathymetric effect on P wave excitation should be considered (in the previous analysis for single point locations, the consideration of bathymetric effect is unnecessary because a scaling over the source PSD series does not change the value of the correlation coefficient between P_{dmc} and source PSD). Using the equations proposed by Gualtieri et al. (2014) and the bathymetry around NZ (Figure 5a), we compute the bathymetric amplification factors for P waves at a period of 6.2 s (Figure 5b; see Figure S3 for comparisons between the factors calculated following Longuet-Higgins, 1950, and Gualtieri et al., 2014). The factors vary largely with locations. Also, note that the P_{dmc} phase has different sensitivity to the sources in the effective region, or, say, the sources make varying contributions to the P_{dmc} signal. The power of sources should be weighted in the averaging. We obtain the weights by backprojecting the beam power of noise correlations onto a global grid (Figure 5c; see supporting information for technical details). Figure 5d shows the map of annually averaged source PSDs surrounding NZ, and Figure 5e shows the map after the modulation of the bathymetric amplification factors in Figure 5b. The spatial patterns are altered significantly, indicating
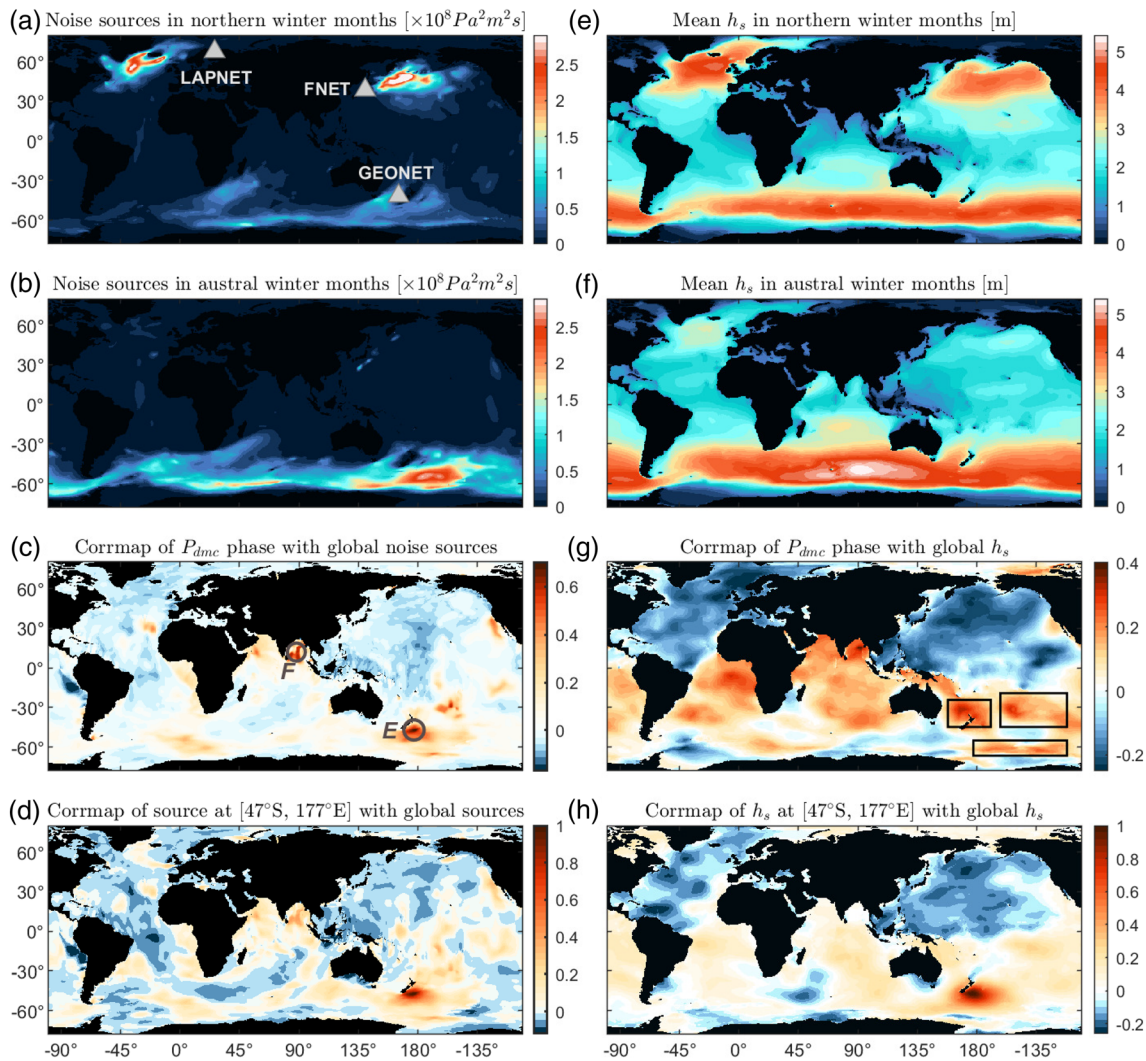
Figure 3. (a) Global map of average PSD of oceanic microseism sources in 2008 northern winter months (January to March and October to December), for a seismic perod of 6.2 s. (b) Similar to (a) but for 2008 austral winter months (April to September). (c) Correlation map (corrmap) for the P_{dmc} strength and global microseism noise sources. Circles mark two regions with highest correlation coefficients: E, effective source region surrounding [47°S, 177°E] south of NZ; F, fake highly correlated region surrouding [12°N, 88°E] in the Bay of Bengal. (d) Correlation map for the source at [47°S, 177°E] and global sources. (e) Mean significant wave height (h_s; 4 times the square root of the zeroth-order moment of ocean wave frequency spectrum) in northern winter months. (f) Similar to (e) but for austral winter months. (g) Correlation map for the P_{dmc} strength and global wave heights. (h) Correlation map for wave heights at [47°S, 177°E] and global wave heights. The oceanographical hindcast data are provided by the IOWAGA products (Rascle & Ardhuin, 2013).

the importance to account for the bathymetric effect. The final source imaging that has been weighted by Figure 5c is plotted in Figure 5f. It agrees well with the effective source region E determined from the correlation map in Figure 3c. Replacing the annual PSD map in Figure 5d with daily PSD maps, we obtain maps like Figure 5f for each date. Averaging over the map leads to the time series of daily intensity in the effective source region (labeled as effective source intensity in Figure 6). Averaging over a wide region has the advantage that the effects of potential source location errors due to the simplification of Earth model for fast travel time calculation, which have been addressed in some single array backprojection studies (e.g., Gal et al., 2015; Nishida & Takagi, 2016), can be largely reduced. From Figure 6, one can see that the new effective source intensity series has almost the same peaks as the source PSD series for [47°S, 177°E] in Figure 4b, suggesting that the observed peak disparities are caused by other reasons. Next, we investigate if the disparities are caused by errors in the simulation of hindcast data or if there are other physical explanations.
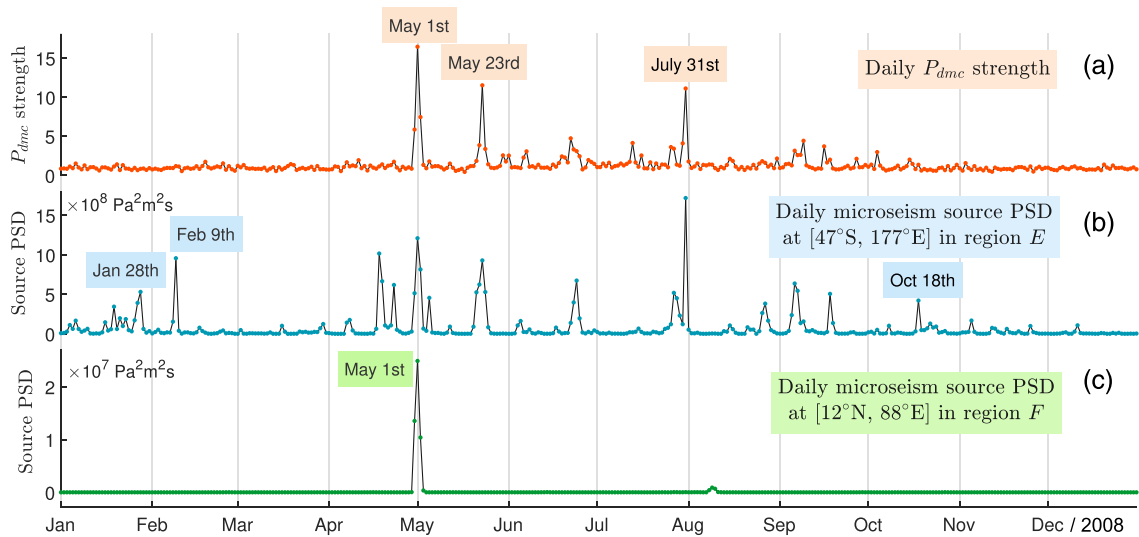
Figure 4. True correlation ($r = 0.73$) between (a) the P_{dmc} strength from Figure 2 and (b) the power of source at [47°S, 177°E] in the effective source region (E in Figure 3c), and spurious correlation ($r = 0.71$) between P_{dmc} and (c) the power of source at [12°N, 88°E] in the Bay of Bengal (F in Figure 3c).
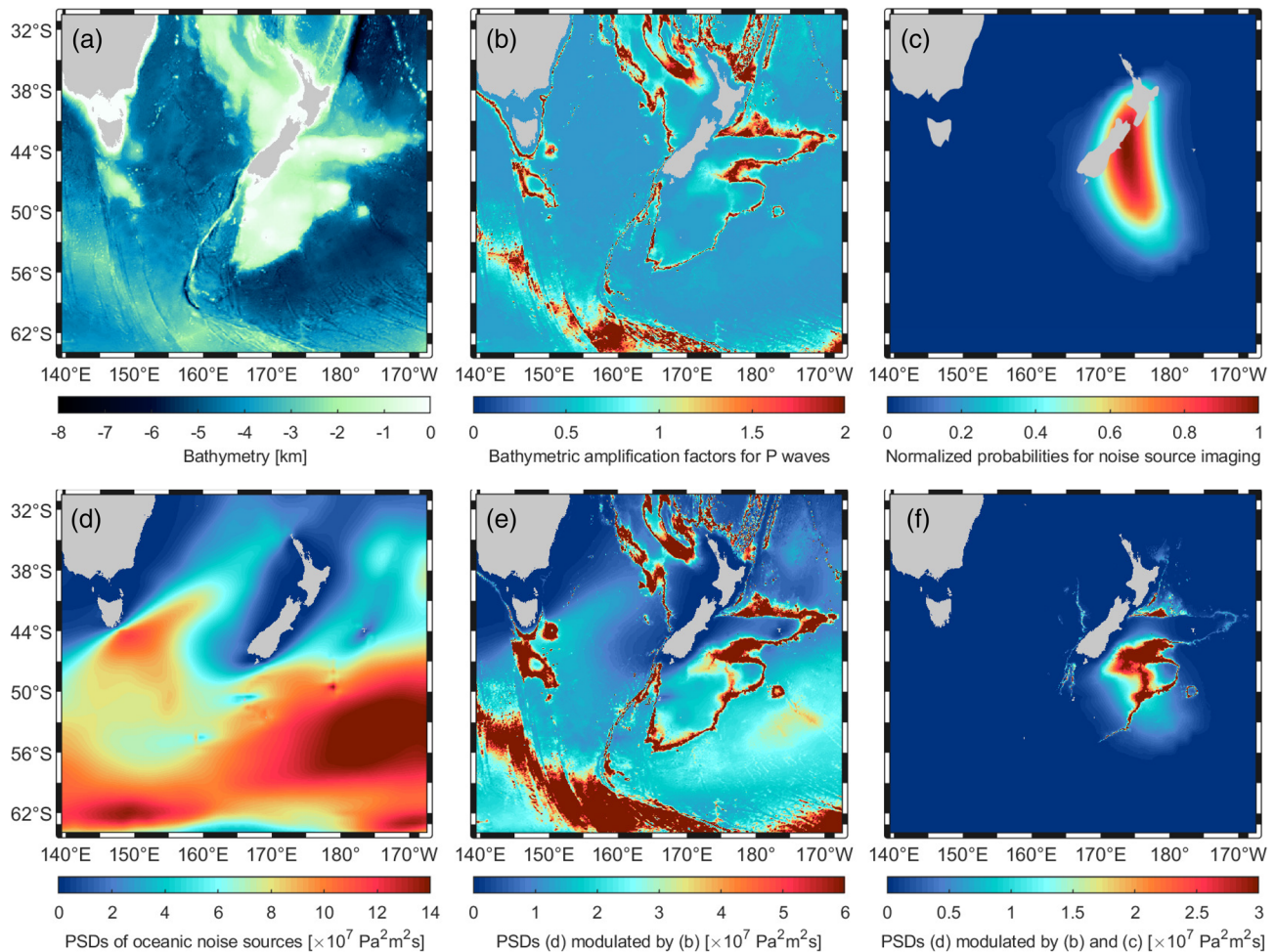

Figure 5. (a) Bathymetry around NZ. (b) Bathymetric amplification factors for P-type waves. (c) Imaging of effective sources obtained from the backprojection of the FNET-LAPNET noise correlations. (d) Annual average of source PSDs in 2008. (e) Source PSDs in (d) modulated by the factors in (b). (f) Source PSDs in (e) further modulated by the weights in (c).
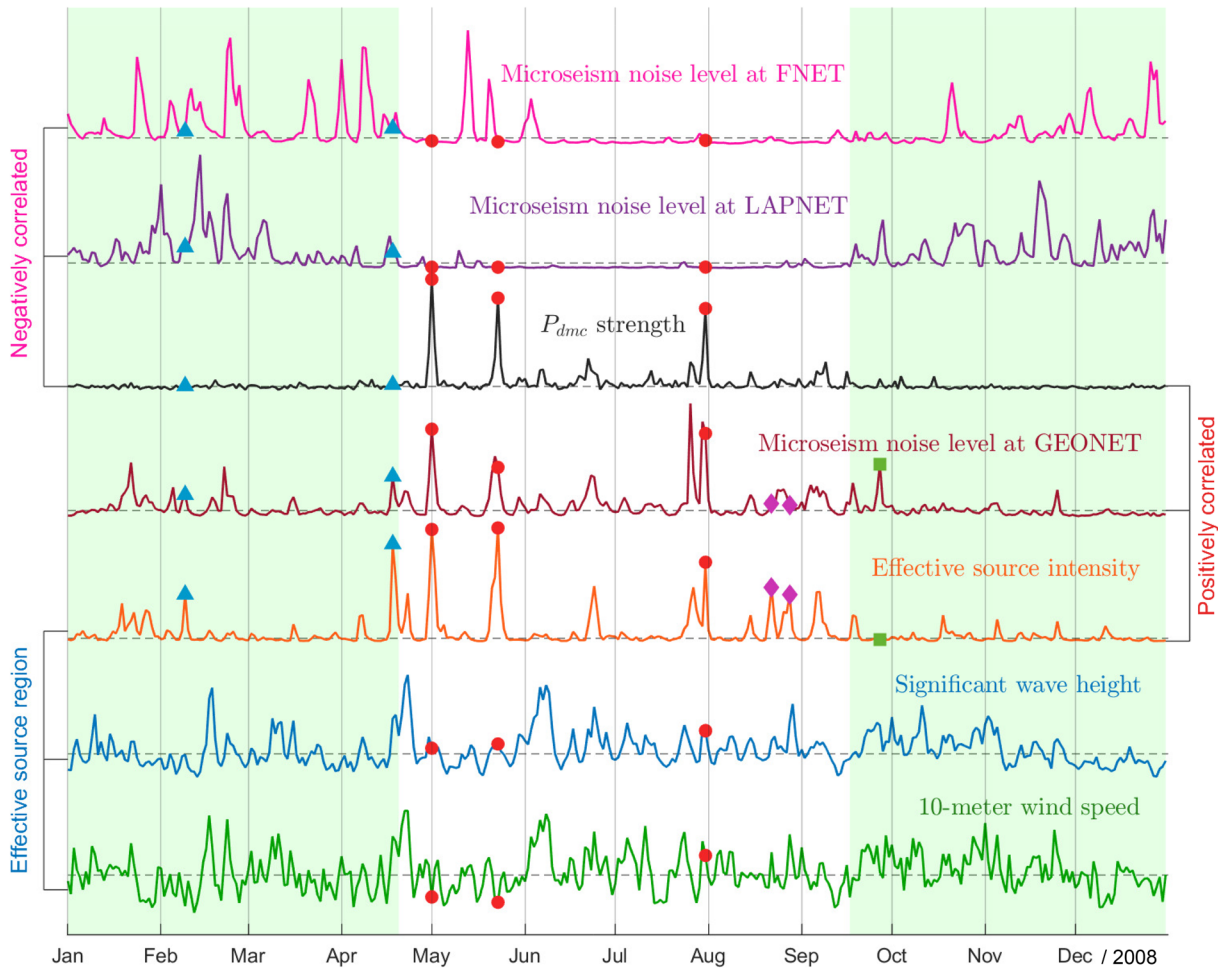
Figure 6. Temporal variations of daily P_{dmc} strength, microseism noise levels at three networks, and average wind speeds, wave heights, and microseism excitations in the effective source region. The curves are normalized by their own maximums. Dashed horizontal lines denote their respective medians. Symbols mark some dates cited in the main text. When computing the effective source intensity, the bathymetric factors in Figure 5b and weights in Figure 5c are used. When computing the average wind speeds and wave heights, weights in Figure 5c are used.

The microseism source PSD data are simulated from the hindcast data of ocean wave directional spectra base on the excitation theory of Longuet-Higgins (1950) and Hasselmann (1963), which have no constrains from seismological observations. One should consider the accuracy of the simulation: Can we ascribe the peak disparities in Figure 4 to the simulation error or not? The seismic noise records from the GEONET array adjacent to the effective source region provide the opportunity to validate the simulation. To obtain the daily microseism noise levels at GEONET, we apply the Hampel filter, a variant of the classic median filter, to the continuous seismograms to discard earthquakes and anomalous impulses. The filter replaces outliers with the medians of the outliers' neighbors and retains the normal samples. Technical details are provided in Text S4 of the supporting information. The resultant GEONET noise level exhibits a good correlation with the effective source intensity ($r = 0.7$). We thus deem that the numerical simulations are statistically reliable. When the effective source intensity is high, the GEONET noise level should also be high (e.g., see the peaks marked by dots in Figure 6). However, due to the great spatiotemporal variability of noise sources in the effective region and the complexity of seismic waves propagating from ocean to land (Gualtieri et al., 2015; Ying et al., 2014), a larger peak in the source intensity series does not necessarily imply a larger peak in the noise level time series (e.g., see diamonds in Figure 6). We also emphasize that a high GEONET noise level does not need to always have a correspondence in the source intensity (e.g., see squares in Figure 6), because the GEONET stations record microseisms emanating from noise sources all around and not only from the effective source region.
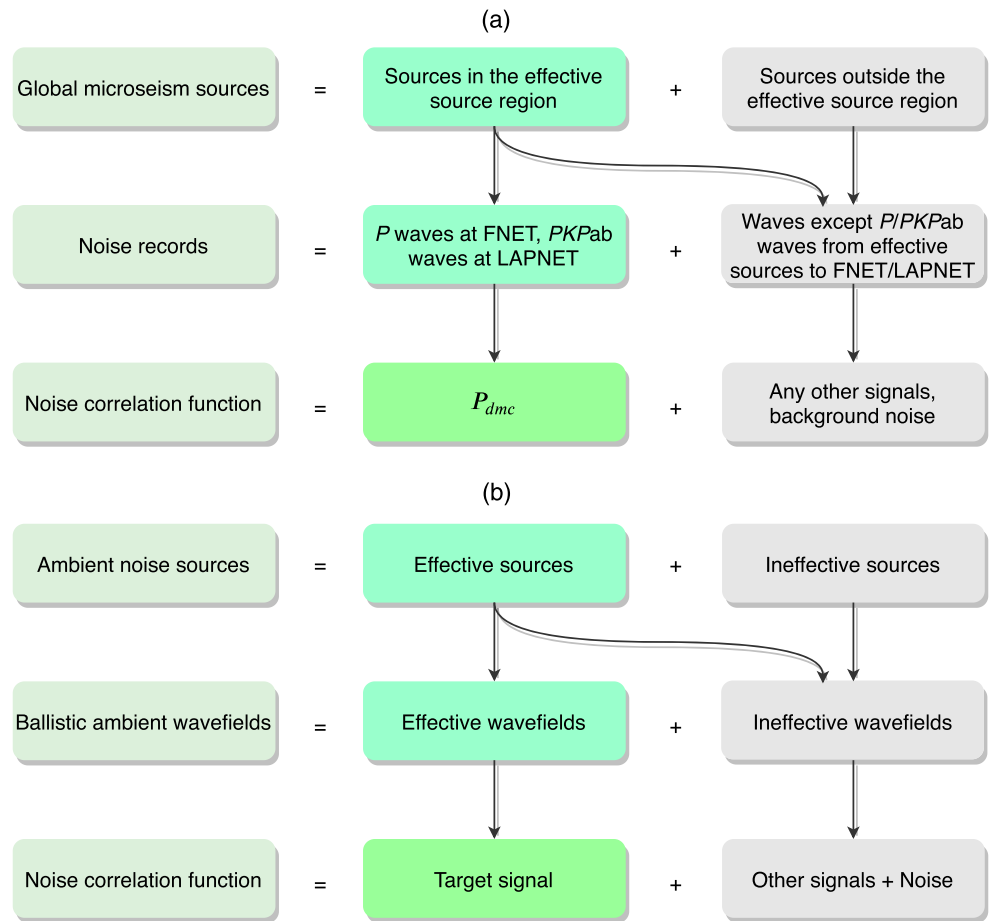
(a)

Global microseism sources	=	Sources in the effective source region	+	Sources outside the effective source region
Noise records	=	P waves at FNET, *PKP*ab waves at LAPNET	+	Waves except *P/PKP*ab waves from effective sources to FNET/LAPNET
Noise correlation function	=	P_{dmc}	+	Any other signals, background noise

(b)

Ambient noise sources	=	Effective sources	+	Ineffective sources
Ballistic ambient wavefields	=	Effective wavefields	+	Ineffective wavefields
Noise correlation function	=	Target signal	+	Other signals + Noise

Figure 7. (a) Sketch explanation for the relationships between microseism noise sources and the noise-derived P_{dmc} signal. (b) Generalization of diagram (a) for an arbitrary signal derived from ambient noise wavefields that are dominated by ballistic waves.

The above analysis explains the observed disparities between the P_{dmc} strength and the effective source intensity. From Figure 6, one can see that the disparities primarily emerge in the shaded period when dominant microseism sources shift to the Northern Hemisphere. The shading roughly separates the northern winter from the austral winter. The correlation between P_{dmc} strength and effective source intensity is low in the shaded period ($r = 0.16$), in contrast to the high correlation during the unshaded period ($r = 0.74$). Large P_{dmc} peaks always emerge on dates during the austral winter when the effective source intensity is much higher than its median, and meanwhile, noise levels at FNET and LAPNET are below their respective medians (e.g., see dots in Figure 6). The seasonal variations of oceanic sources in the Southern Hemisphere are less strong than in the Northern Hemisphere (Figure 3). On some dates (e.g., see triangles in Figure 6), the effective source intensity can be considerable, but relevant P_{dmc} peaks are still missing. We notice that the corresponding microseism levels at FNET and LAPNET are obviously above their medians. Intensive ocean activity and microseism excitations in the North Pacific and Atlantic lead to increased microseism noise levels at FNET and LAPNET. The P_{dmc} strength is anticorrelated with microseism noise levels at FNET ($r = -0.12$) and LAPNET ($r = -0.18$). We hereby conjecture that the microseism energy from the distant effective source region is dwarfed by the energetic microseisms excited by oceanic sources closer to the correlated FNET and LAPNET arrays, and consequently, P_{dmc} signals are overwhelmed by the background noise in the FNET-LAPNET cross correlations. Last, we mention that the median threshold in Figure 6 separates the major features of the time series described above, but there is no guarantee that it is a perfect threshold due to the nonlinear relationships between the P_{dmc} strength and the noise levels at the arrays.

5. Discussions and Conclusions

In this study, we explore the relations between the noise-derived P_{dmc} signals and global oceanic microseism sources using spatiotemporal correlation analysis. The effective source region E for the P_{dmc} phase is successfully identified from the correlation map in Figure 3c, which is consistent with that determined from the seismological backprojection in Figure 5c. The correlation map provides a convenient way to identify the effective sources of noise-derived seismic signals.

In our case, the seismic networks used for noise correlation are located in the Northern Hemisphere, while the effective source region is in the Southern Hemisphere. Ideally, we expect a correlation map with the following features: positive correlation with sources in the effective region and negative or insignificant correlations with other inefficient sources. Positive correlation indicates a contribution to the construction of P_{dmc} signal from noise correlations, negative correlation implies an adverse impact, and insignificant correlation (decorrelation) means a negligible effect on the signal construction. However, we obtained a correlation map roughly showing that the P_{dmc} signal is correlated with the southern sources and anticorrelated with the northern sources. The correlation with southern sources outside the effective region can be interpreted with the spatiotemporal correlation of the power of the microseism sources in the southern oceans, due to the large span of ocean storms and the long-range propagation of swells. The anticorrelation with the northern sources can partly be explained by the well-known reverse seasonal patterns of oceanic microseism excitations in the Southern and Northern Hemispheres (Hillers et al., 2012; Landès et al., 2010; Reading et al., 2014; Stutzmann et al., 2009). Another important reason is that compared to the remote effective sources in the Southern Hemisphere, the northern sources closer to the correlated stations have larger impacts on the microseism noise levels at stations. Strong energy flux from the northern sources outshines the microseism energy coming from the distant effective sources. That deteriorates the construction of the P_{dmc} phase. The noise-derived P_{dmc} signals are primarily observable in the austral winter. That can be, on the one hand, attributed to the stronger effective source intensity during that period and, on the other hand, to the relative tranquility in the northern oceans.

In Figure 7, we summarize the classification of noise sources, the decomposition of wavefields, and the associations to the constituents of the interreceiver noise correlation function. The diagram of Figure 7a explains the relationships using the case study of the P_{dmc} phase discussed above. We generalize Figure 7a to the derivation of an arbitrary signal (referred to as the target signal for convenience) from ambient noise wavefields (Figure 7b). The noise correlation function is composed of the target signal, any other signals, and background noise. A source or a wave is called effective if it contributes to the construction of the target signal from noise correlations. Otherwise, it is called ineffective. The construction of the target signal is exclusively ascribed to the interference between the effective waves. Stronger effective sources (relative to ineffective sources) imply more effective waves in the total wavefield and, thereby, a better quality for the noise-derived target signal. Note that not all waves emanating from the effective sources, but only those following specific ray paths, are effective. There might be multiple pairs of seismic phases that could contribute to the construction of the target signal. However, their relative strength matters. As for the case of the P_{dmc} phase, the effective waves are P and $PKPab$, which are both prominent phases in the ballistic wavefield. Li et al. (2020) showed that the PcP-$PKPab$ correlation and the PcS-$PcPPcP$ correlation could also lead to a signal at around the P_{dmc} emerging time. However, the PcP, PcS, and $PcPPcP$ waves are weak phases in the ballistic wavefield and thereby have minor contributions to the P_{dmc} signals. We emphasize that the sketch in Figure 7b is only suitable for the ambient noise wavefields that are dominated by ballistic waves.

From Figure 6, one can observe a high correlation between wind speed and wave height in region E ($r = 0.74$). It indicates that the ocean waves in region E are likely dominated by the waves forced by local winds. The correlation between wave height and microseism excitation is low ($r = 0.25$), implying a dominant role of the freely propagating swells in exciting the microseisms. Extreme sea state does not guarantee strong microseism excitation. That is not surprising according to the microseism excitation theory (Hasselmann, 1963; Longuet-Higgins, 1950): The excitation is proportional to the product of the heights of the colliding equal-frequency ocean waves. In lack of equal-frequency waves coming from opposite directions, even extreme wave climate cannot incite strong secondary microseisms. In contrast, for large peaks in the microseism excitation, the corresponding wave heights are generally moderate (e.g., on 1 and 23 May). On these two dates, the low wind speeds but moderate wave heights in region E suggest that the

ocean waves are dominantly the freely traveling swells from elsewhere, as also illustrated in the supporting information Movie S1. Oppositely propagating equal-frequency swells collide with each other and incite strong microseisms. Our analysis and observations agree with those of Obrebski et al. (2012), who investigated a specific case that small swells from two storms meeting in the eastern Pacific generate loud microseism noise. There are also examples showing that wind waves can play a role in the excitation of microseisms, for instance, around 31 July when the local winds, wave height, and microseism excitations are all strong. Such examples are few. The good consistency between the temporal variations in the P_{dmc} strength, the effective source intensity, and the NZ microseism noise level (Figure 6), provides extra support to the analysis of the P_{dmc} observations and the quasi-stationary phase arguments proposed by Li et al. (2020). It also gives credit to the validity of the numerical modeling of oceanic microseism sources by Ardhuin et al. (2011) and Rascle and Ardhuin (2013).

We have described above the implications of this study in seismology and in understanding the process of microseism excitation. Now, we discuss the significance in oceanography and climate science. Well-documented historical ocean storms and wave climate are valuable for improving our understanding of climate change and global warming (Ebeling, 2012). However, modern satellite observations of ocean waves and storms have a history of merely decades. Microseisms are induced by storm-driven ocean waves (Ardhuin et al., 2015; Hasselmann, 1963; Longuet-Higgins, 1950). The records of microseisms contain the imprint of climate (Aster et al., 2010; Stutzmann et al., 2009). Instrumental observation of microseisms has an over-century history and started much earlier than the modern observations of ocean waves and storms. It has been a long-lasting effort for the seismological community to digitalize the historical analog seismograms (Bogiatzis & Ishii, 2016; Lecocq et al., 2020). Researchers expect that past seismic records can be used to recover undocumented historical ocean storms and wave climate (Ebeling, 2012; Lecocq et al., 2020).

This study confirms that it is possible to detect remote microseism events (burst of microseism energy) with land observation of microseisms. We demonstrate that the noise-derived P_{dmc} signals can be employed to monitor microseism events in a specific ocean region (Figure 5). The remote monitoring of microseisms is promising as an aid to improving wave hindcast, in similar manners as demonstrated by Stopa et al. (2019). The comparative analysis in Figure 6 indicates that the remote event detection could be effective in the absence of strong sources near the stations; otherwise the detection could fail. Stations at low latitudes where wave climate and microseism excitation are relatively mild, or inland stations far from oceans, should have better performance in remote monitoring.

Energetic microseism excitation does not always need extreme in situ wave heights, and extreme wave heights do not necessarily produce powerful microseisms (Obrebski et al., 2012; and this study). It implies that secondary microseism events are not a perfect proxy for the extremal in situ wave climate. However, it does not mean the long-lasting attempt to monitor remote sea state and ocean storms with land observation of secondary microseisms is futile. In the P_{dmc}-h_s correlation map (Figure 3g), the largest r values do not fall in the effective region E as in the P_{dmc}-source correlation map (Figure 3c) but in surrounding regions with moderate to high ocean wave activity (the bounded areas in Figure 3g). We speculate that these regions could be the birthplaces of the colliding swells that generate the secondary microseisms in region E, or the ocean waves in these regions are driven by the same storms as the colliding waves in region E (see the spatial links of h_s from Figure 3h and supporting information Movie S1). The detection of a microseism event could affirm the existence of the causative storms that generated the ocean waves propagating to the location of the microseism event, although the storms could be distant from the events.

Data Availability Statement

The seismic data of FNET and LAPNET were provided by the National Research Institute for Earth Science and Disaster Resilience (http://www.fnet.bosai.go.jp/; last access: June 2018) and the Réseau Sismologique & Géodésique Français (http://www.resif.fr/; last access: June 2018), respectively. The seismic data of GEONET and the earthquake catalog of New Zealand were provided by the GEONET Data Center (https://www.geonet.org.nz/; last access: June 2018). The global earthquake catalog was provided by the U.S. Geological Survey (https://earthquake.usgs.gov/; last access: June 2018). The wind hindcast data were provided by the European Centre for Medium-Range Weather Forecasts (https://www.ecmwf.int/; last

access: June 2018). The hindcast data of wave heights and microseism source PSDs were provided by the IOWAGA products (Rascle & Ardhuin, 2013). The bathymetry data were extracted from ETOPO1 Global Relief Model (Amante & Eakins, 2009).

References

Amante, C., & Eakins, B. W. (2009). ETOPO1 1 Arc-Minute Global Relief Model: Procedures, data sources and analysis. *NOAA Technical Memorandum NESDIS NGDC-24.* https://doi.org/10.7289/V5C8276M

Ardhuin, F., Chapron, B., & Collard, F. (2009). Observation of swell dissipation across oceans. *Geophysical Research Letters*, *36*, L06607. https://doi.org/10.1029/2008GL037030

Ardhuin, F., Gualtieri, L., & Stutzmann, E. (2015). How ocean waves rock the Earth: Two mechanisms explain microseisms with periods 3 to 300s. *Geophysical Research Letters*, *42*, 765–772. https://doi.org/10.1002/2014GL062782

Ardhuin, F., Stutzmann, E., Schimmel, M., & Mangeney, A. (2011). Ocean wave sources of seismic noise. *Journal of Geophysical Research*, *116*, C09004. https://doi.org/10.1029/2011JC006952

Aster, R. C., McNamara, D. E., & Bromirski, P. D. (2010). Global trends in extremal microseism intensity. *Geophysical Research Letters*, *37*, L14303. https://doi.org/10.1029/2010GL043472

Bernard, P. (1990). Historical sketch of microseisms from past to future. *Physics of the Earth and Planetary Interiors*, *63*(3–4), 145–150. https://doi.org/10.1016/0031-9201(90)90013-N

Bogiatzis, P., & Ishii, M. (2016). DigitSeis: A new digitization software for analog seismograms. *Seismological Research Letters*, *87*(3), 726–736. https://doi.org/10.1785/0220150246

Boué, P., Poli, P., Campillo, M., Pedersen, H., Briand, X., & Roux, P. (2013). Teleseismic correlations of ambient seismic noise for deep global imaging of the Earth. *Geophysical Journal International*, *194*(2), 844–848. https://doi.org/10.1093/gji/ggt160

Boué, P., Poli, P., Campillo, M., & Roux, P. (2014). Reverberations, coda waves and ambient noise: Correlations at the global scale and retrieval of the deep phases. *Earth and Planetary Science Letters*, *391*, 137–145. https://doi.org/10.1016/j.epsl.2014.01.047

Campillo, M., & Paul, A. (2003). Long-range correlations in the diffuse seismic coda. *Science*, *299*(5606), 547–549. https://doi.org/10.1126/science.1078551

Dewey, J., & Byerly, P. (1969). The early history of seismometry (to 1900). *Bulletin of the Seismological Society of America*, *59*(1), 183–227.

Ebeling, C. W. (2012). Inferring ocean storm characteristics from ambient seismic noise. In R. Dmowska (Ed.), *Advances in geophysics* (Vol. 53, pp. 1–33). New York: Elsevier. https://doi.org/10.1016/B978-0-12-380938-4.00001-X

Euler, G. G. G., Wiens, D. D. A., & Nyblade, A. A. (2014). Evidence for bathymetric control on the distribution of body wave microseism sources from temporary seismic arrays in Africa. *Geophysical Journal International*, *197*(3), 1869–1883. https://doi.org/10.1093/gji/ggu105

Gal, M., Reading, A. M., Ellingsen, S. P., Gualtieri, L., Koper, K. D., Burlacu, R., et al. (2015). The frequency dependence and locations of short-period microseisms generated in the Southern Ocean and west Pacific. *Journal of Geophysical Research: Solid Earth*, *120*, 5764–5781. https://doi.org/10.1002/2015JB012210

Gerstoft, P., Shearer, P. M., Harmon, N., & Zhang, J. (2008). Global P, PP, and PKP wave microseisms observed from distant storms. *Geophysical Research Letters*, *35*, L23306. https://doi.org/10.1029/2008GL036111

Gualtieri, L., Stutzmann, E., Capdeville, Y., Farra, V., Mangeney, A., & Morelli, A. (2015). On the shaping factors of the secondary microseismic wavefield. *Journal of Geophysical Research: Solid Earth*, *2*, 6241–6262. https://doi.org/10.1029/2000GC000119

Gualtieri, L., Stutzmann, E., Farra, V., Capdeville, Y., Schimmel, M., Ardhuin, F., & Morelli, A. (2014). Modelling the ocean site effect on seismic noise body waves. *Geophysical Journal International*, *197*(2), 1096–1106. https://doi.org/10.1093/gji/ggu042

Harrison, E. P. (1924). Microseisms and storm forecasts. *Nature*, *114*(2870), 645–645. https://doi.org/10.1038/114645b0

Hasselmann, K. (1963). A statistical analysis of the generation of microseisms. *Reviews of Geophysics*, *1*(2), 177–210. https://doi.org/10.1029/RG001i002p00177

Hillers, G., Graham, N., Campillo, M., Kedar, S., Landès, M., & Shapiro, N. (2012). Global oceanic microseism sources as seen by seismic arrays and predicted by wave action models. *Geochemistry, Geophysics, Geosystems*, *13*, Q01021. https://doi.org/10.1029/2011GC003875

Kedar, S., Longuet-Higgins, M., Webb, F., Graham, N., Clayton, R., & Jones, C. (2008). The origin of deep ocean microseisms in the North Atlantic Ocean. *Proceedings of the Royal Society A: Mathematical, Physical and Engineering Sciences*, *464*(2091), 777–793. https://doi.org/10.1098/rspa.2007.0277

Landès, M., Hubans, F., Shapiro, N. M., Paul, A., & Campillo, M. (2010). Origin of deep ocean microseisms by using teleseismic body waves. *Journal of Geophysical Research*, *115*, B05302. https://doi.org/10.1029/2009JB006918

Lecocq, T., Ardhuin, F., Collin, F., & Camelbeeck, T. (2020). On the extraction of microseismic ground motion from analog seismograms for the validation of ocean-climate models. *Seismological Research Letters*, *91*(3), 1518–1530. https://doi.org/10.1785/0220190276

Li, L., Boué, P., & Campillo, M. (2020). Observation and explanation of spurious seismic signals emerging in teleseismic noise correlations. *Solid Earth*, *11*(1), 173–184. https://doi.org/10.5194/se-11-173-2020

Lin, F. C., & Tsai, V. C. (2013). Seismic interferometry with antipodal station pairs. *Geophysical Research Letters*, *40*(17), 4609–4613. https://doi.org/10.1002/grl.50907

Lin, F. C., Tsai, V. C., Schmandt, B., Duputel, Z., & Zhan, Z. (2013). Extracting seismic core phases with array interferometry. *Geophysical Research Letters*, *40*(6), 1049–1053. https://doi.org/10.1002/grl.50237

Liu, Q., Koper, K. D., Burlacu, R., Ni, S., Wang, F., Zou, C., et al. (2016). Source locations of teleseismic *P*, SV, and SH waves observed in microseisms recorded by a large aperture seismic array in China. *Earth and Planetary Science Letters*, *449*, 39–47. https://doi.org/10.1016/j.epsl.2016.05.035

Longuet-Higgins, M. S. (1950). A theory of the origin of microseisms. *Philosophical Transactions of the Royal Society A: Mathematical, Physical and Engineering Sciences*, *243*(857), 1–35. https://doi.org/10.1098/rsta.1950.0012

Meschede, M., Stutzmann, E., Farra, V., Schimmel, M., & Ardhuin, F. (2017). The effect of water column resonance on the spectra of secondary microseism *P* waves. *Journal of Geophysical Research: Solid Earth*, *122*, 8121–8142. https://doi.org/10.1002/2017JB014014

Meschede, M., Stutzmann, E., & Schimmel, M. (2018). Blind source separation of temporally independent microseisms. *Geophysical Journal International*, *216*(2), 1260–1275. https://doi.org/10.1093/gji/ggy437

Nishida, K. (2013). Global propagation of body waves revealed by cross-correlation analysis of seismic hum. *Geophysical Research Letters*, *40*, 1691–1696. https://doi.org/10.1002/grl.50269

Nishida, K., & Takagi, R. (2016). Teleseismic S wave microseisms. *Science*, *353*(6302), 919–921. https://doi.org/10.1126/science.aaf7573

Obrebski, M. J., Ardhuin, F., Stutzmann, E., & Schimmel, M. (2012). How moderate sea states can generate loud seismic noise in the deep ocean. *Geophysical Research Letters*, *39*, L11601. https://doi.org/10.1029/2012GL051896

Peterson, J. (1993). Observations and modeling of seismic background noise. U.S. Geol. Surv. Open File Report 93–322. https://doi.org/10.3133/ofr93322

Phạm, T. S., Tkalčić, H., Sambridge, M., & Kennett, B. L. N. (2018). Earth's correlation wavefield: Late coda correlation. *Geophysical Research Letters*, *45*, 3035–3042. https://doi.org/10.1002/2018GL077244

Poli, P., Thomas, C., Campillo, M., & Pedersen, H. A. (2015). Imaging the D″ reflector with noise correlations. *Geophysical Research Letters*, *42*, 60–65. https://doi.org/10.1002/2014GL062198

Rascle, N., & Ardhuin, F. (2013). A global wave parameter database for geophysical applications. Part 2: Model validation with improved source term parameterization. *Ocean Modelling*, *70*, 174–188. https://doi.org/10.1016/j.ocemod.2012.12.001

Reading, A. M., Koper, K. D., Gal, M., Graham, L. S., Tkalčić, H., & Hemer, M. A. (2014). Dominant seismic noise sources in the Southern Ocean and west Pacific, 2000–2012, recorded at the Warramunga Seismic Array, Australia. *Geophysical Research Letters*, *41*, 3455–3463. https://doi.org/10.1002/2014GL060073

Retailleau, L., Boué, P., Li, L., & Campillo, M. (2020). Ambient seismic noise imaging of the lowermost mantle beneath the North Atlantic Ocean. *Geophysical Journal International*, *222*(2), 1339–1351. https://doi.org/10.1093/gji/ggaa210

Retailleau, L., & Gualtieri, L. (2019). Toward high-resolution period-dependent seismic monitoring of tropical cyclones. *Geophysical Research Letters*, *46*, 1329–1337. https://doi.org/10.1029/2018GL080785

Rost, S., & Thomas, C. (2002). Array seismology: Methods and applications. *Reviews of Geophysics*, *40*(3), 1008. https://doi.org/10.1029/2000RG000100

Shapiro, N. M., & Campillo, M. (2004). Emergence of broadband Rayleigh waves from correlations of the ambient seismic noise. *Geophysical Research Letters*, *31*, L07614. https://doi.org/10.1029/2004GL019491

Spica, Z., Perton, M., & Beroza, G. C. (2017). Lateral heterogeneity imaged by small-aperture ScS retrieval from the ambient seismic field. *Geophysical Research Letters*, *44*, 8276–8284. https://doi.org/10.1002/2017GL073230

Stehly, L., Campillo, M., & Shapiro, N. M. (2006). A study of the seismic noise from its long-range correlation properties. *Journal of Geophysical Research*, *111*, B10306. https://doi.org/10.1029/2005JB004237

Steim, J. M. (2015). Theory and observations—Instrumentation for global and regional seismology. In *Treatise on geophysics* (pp. 29–78). New York: Elsevier. https://doi.org/10.1016/B978-0-444-53802-4.00023-3

Stopa, J. E., Ardhuin, F., Stutzmann, E., & Lecocq, T. (2019). Sea state trends and variability: Consistency between models, altimeters, buoys, and seismic data (1979–2016). *Journal of Geophysical Research: Oceans*, *124*, 3923–3940. https://doi.org/10.1029/2018jc014607

Stutzmann, E., Ardhuin, F., Schimmel, M., Mangeney, A., & Patau, G. (2012). Modelling long-term seismic noise in various environments. *Geophysical Journal International*, *191*(2), 707–722. https://doi.org/10.1111/j.1365-246X.2012.05638.x

Stutzmann, E., Schimmel, M., Patau, G., & Maggi, A. (2009). Global climate imprint on seismic noise. *Geochemistry, Geophysics, Geosystems*, *10*, Q11004. https://doi.org/10.1029/2009GC002619

Turner, R. J., Gal, M., Hemer, M. A., & Reading, A. M. (2020). Impacts of the cryosphere and atmosphere on observed microseisms generated in the Southern Ocean. *Journal of Geophysical Research: Earth Surface*, *125*(2), e2019JF005354. https://doi.org/10.1029/2019JF005354

Xia, H. H., Song, X., & Wang, T. (2016). Extraction of triplicated PKP phases from noise correlations. *Geophysical Journal International*, *205*(1), 499–508. https://doi.org/10.1093/gji/ggw015

Ying, Y., Bean, C. J., & Bromirski, P. D. (2014). Propagation of microseisms from the deep ocean to land. *Geophysical Research Letters*, *41*, 6374–6379. https://doi.org/10.1002/2014GL060979

Zhang, J., Gerstoft, P., & Shearer, P. M. (2010). Resolving P-wave travel-time anomalies using seismic array observations of oceanic storms. *Earth and Planetary Science Letters*, *292*(3–4), 419–427. https://doi.org/10.1016/j.epsl.2010.02.014

Spatiotemporal correlation analysis of noise-derived seismic body waves with ocean wave climate and microseism sources

Lei Li[1,2], Pierre Boué[2], Lise Retailleau[3,4], Michel Campillo[2]

[1]State Key Laboratory of Earthquake Dynamics, Institute of Geology, CEA, Beijing 100029, China
[2]Univ. Grenoble Alpes, Univ. Savoie Mont Blanc, CNRS, IRD, IFSTTAR, ISTerre, 38000 Grenoble, France
[3]Université de Paris, Institut de physique du globe de Paris, CNRS, F-75005 Paris, France
[4]Observatoire Volcanologique du Piton de la Fournaise, Institut de physique du globe de Paris, F-97418 La Plaine des Cafres, France

Contents of this file

Additional Supporting Information (Files uploaded separately)

Text S1. FNET-LAPNET noise correlations

The correlation function C_{AB} between two seismograms (S_A and S_B) is given by

$$C_{AB}(\tau) = \frac{\sum_i S_A(i)S_B(i-\tau)}{\sqrt{\sum_i S_A^2(i) \sum_i S_B^2(i)}}. \qquad (S1)$$

The resultant C_{AB} consists of an acausal part and a causal part, that correspond to the negative lags ($\tau < 0$) and the positive lags ($\tau > 0$), respectively. For efficiency, it is routine to compute the correlation function with the Fast Fourier Transform:

$$C_{AB}(\tau) = \frac{\mathcal{F}^{-1}[\mathcal{F}(S_A)\mathcal{F}^*(S_B)]}{\sqrt{\sum_i S_A^2(i) \sum_i S_B^2(i)}}. \qquad (S2)$$

Figure S1(a) shows the acausal and causal sections of FNET-LAPNET noise correlations in 2008 that are filtered between 5 s and 10 s and binned in distance intervals of 0.1°. The

acausal section is flipped to share the time axis with the causal section. The expected locations of the acausal and causal noise sources are marked by stars on the maps of global microseism source PSDs and ocean wave heights in Fig. S1(b). The ocean wave activities and microseism excitations at the acausal source region are intense, while those in the causal source region are fainter. Consequently, the P_{dmc} phase is only observable from the acausal noise correlations.
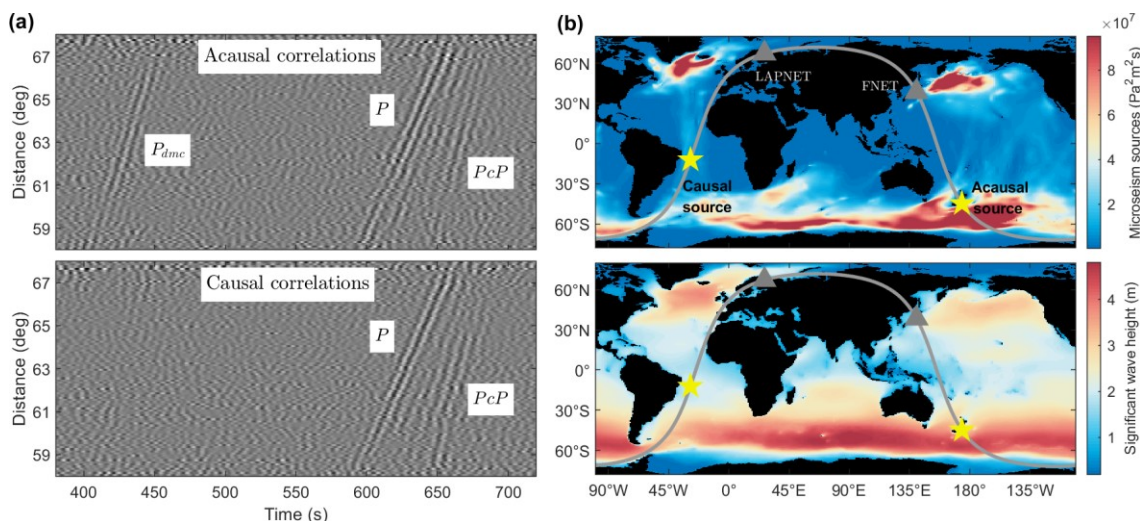

Figure S1. (a) Acausal and causal sections of FNET-LAPNET noise correlations in 2008. (b) Global maps of 6.2 s period secondary microseism sources and significant wave heights in 2008.

Text S2. Noise source imaging by back-projection

Assuming the interferometry between *P* waves at FNET and *PKPab* waves at LAPNET, we image the effective noise sources through the back-projection of the FNET-LAPNET noise correlations. We beam the FNET-LAPNET noise correlations and assign the beam power

$$P_s = \langle\langle C_{ij}(t + t_{si} - t_{sj})\rangle^2_{ij}\rangle_t, \qquad (S3)$$

onto a $0.5° \times 0.5°$ grid as the probabilities of noise sources on the global surface. In the above equation, $\langle\cdot\rangle_x$ means the average over x, C_{ij} is the correlation function between the *i*-th FNET station and the *j*-th LAPNET station, t_{si} is the traveltime of the *P* wave from the *s*-th grid point to the *i*-th FNET station, and t_{sj} is the traveltime of the *PKPab* waves from the *s*-th source to the *j*-th LAPNET station. The inter-station noise correlations are windowed before the beamforming (Fig. S2a). The noise source imaging for the annually stacked noise correlations is plotted in Fig. S2(c). Only the region surrounding NZ is shown. Outside the region, hardly can the *P* wave reach FNET or the *PKPab* waves reach LAPNET. Besides a well-focused imaging of the expected source region in the ocean south of NZ, we notice a secondary spot to the west. In comparisons with the power map of oceanic microseism noise sources in Fig. 5(e), we ascribe it to the strong microseism excitation in the ocean south of Tasmania. We also back-project the daily noise correlations on 2008-05-01 (Fig. S2b), when the P_{dmc} phase reaches the largest strength

through the year (Fig. 2). As shown in Fig. S2(d), an exclusive source region is imaged, which agrees with the dominant spot in Fig. S2(c).
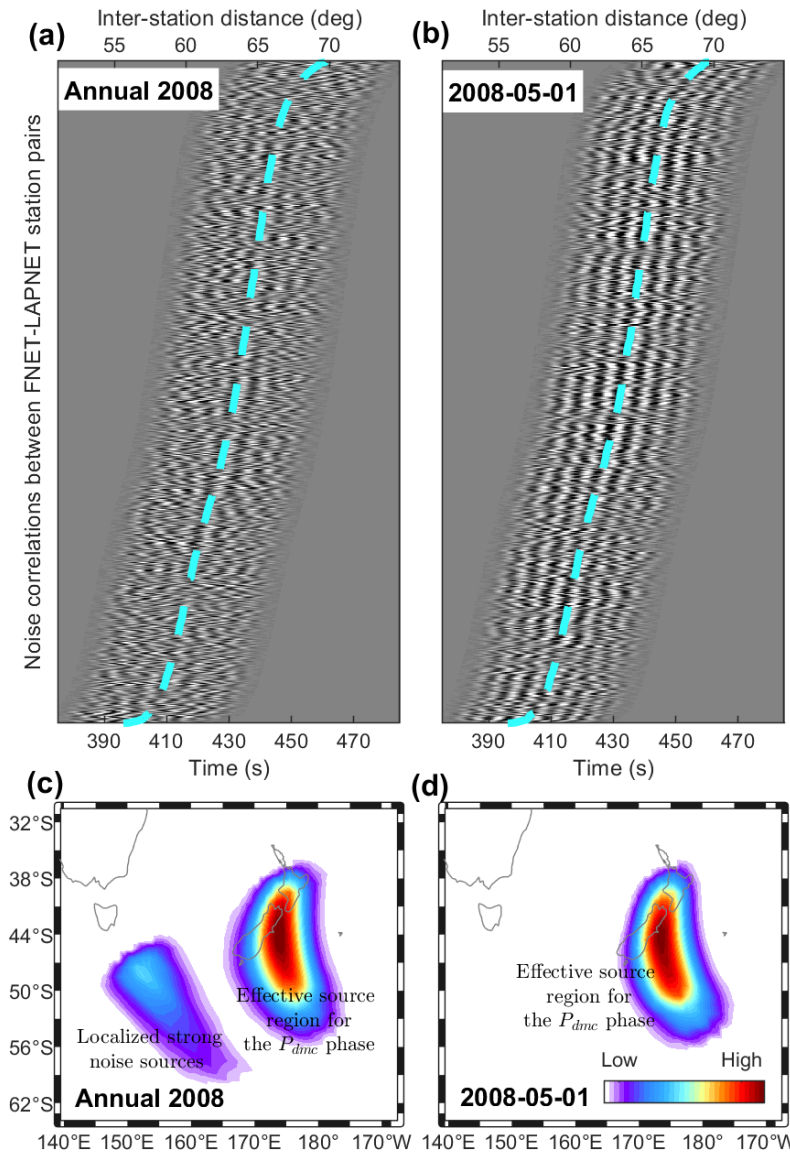

Figure S2. Inter-receiver noise correlations for all FNET-LAPNET station pairs: (a) stacked over the year of 2008; (b) on single day of 2008-05-01. The waveforms are windowed around the P_{dmc} phase. Dashed lines indicate inter-station distances. Back-projection imaging of noise sources: (c) using data from (a); (d) using data from (b).

Text S3. Bathymetric amplification factors

Figure S3 compares the bathymetric amplification factors surrounding New Zealand for P waves and Rayleigh waves. The factors for P waves are computed using the equations proposed by Gualtieri et al. (2014), for a seismic period of 6.2 s and a

3

slowness of 4.6 s/deg. The factors for 6.2 s period Rayleigh waves are obtained by interpolating the table given by Longuet-Higgins (1950).
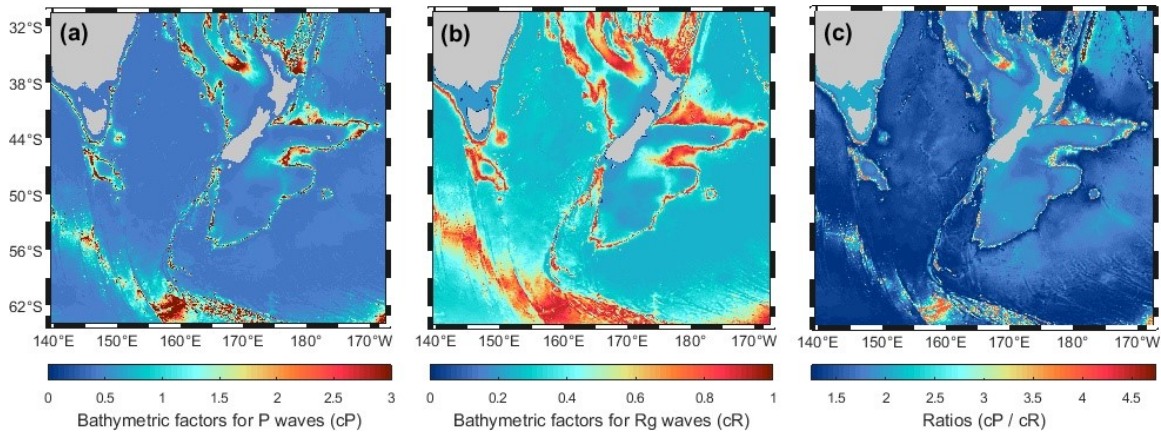

Figure S3. Bathymetric amplification factors for (a) *P* waves and (b) Rayleigh waves. (c) Ratios between the factors for *P* waves and for Rayleigh waves.

Text S4. Microseism noise levels at seismic networks

The continuous seismograms record not only the background vibrations of Earth, but also ground motions induced by seismicity or other events. Instrumental malfunction also leads to anomalous (e.g., nearly vanishing or extremely large) amplitudes in the records. These extreme amplitudes (outliers) could bias the estimates of microseism noise power. It is necessary to get rid of them from the ambient noise records before the computation of noise power. Mean and median filters are the common tools for this task. However, they modify all the samples. Here, we prefer to use a variant of the median filter called Hampel filter. In contrast to the median filter that replace all samples with local medians, the Hampel filter detects outliers by compare a sample with the neighboring samples. A sample is replaced by the local median if it deviates k times of the median absolute deviation (MAD) from the local median, or else, it is unchanged.

We filter the vertical components of the continuous seismograms around 6.2 s period. The seismograms are then divided into 15-min segments and the power of segments is computed. We apply the Hampel filter to the time series of noise power recursively. For each sample, we compute the local median and MAD of its eight neighbors (four before and four after). A sample is replaced by the median if it deviates from the median over three times of the MAD. The de-spiked time series is resampled from a 15-min interval to a 1-hour interval, by averaging over every four samples. Then, we apply the Hampel filter again and resample the time series to a 24-hour interval. The averaging of noise levels over all stations of a seismic network leads to the time series of array noise level. Before the averaging, the Hampel filter is applied again, to discard possible anomalous values at some stations (see Fig. S3 for the example of GEONET). The final time series of microseism noise levels for networks FNET, LAPNET and GEONET are shown in Fig. 6.
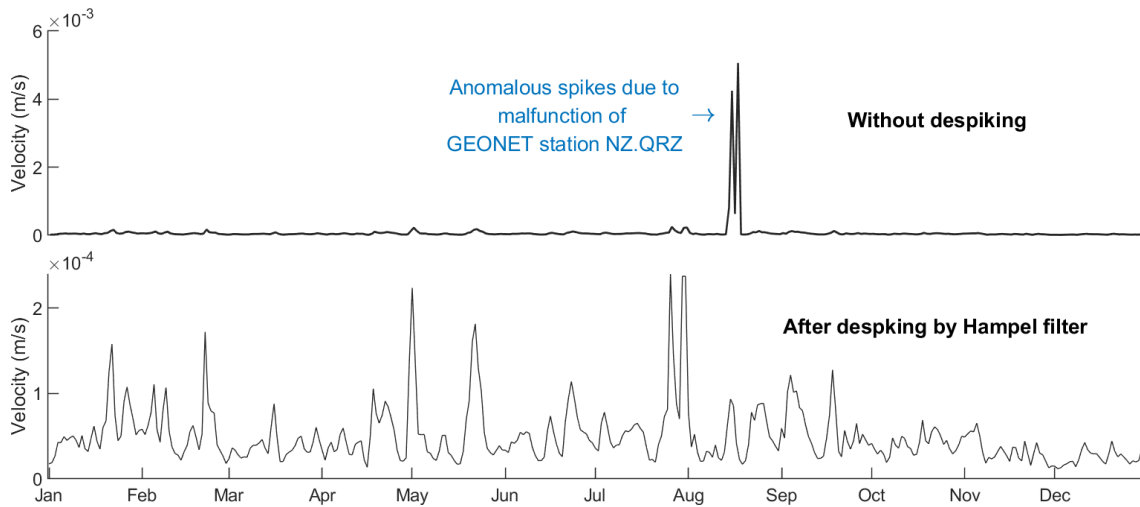
Figure S4. Comparison between the time series of daily GEONET noise levels with (lower) and without (upper) despiking using the Hampel filter.

Table S1. List of earthquakes (magnitude above 5.5) in 2008 extracted from the USGS catalogue, as a supplementary to the comparison between seismicity and P_{dmc} in Fig. 2 of the main text**.** On some dates with earthquakes near the FNET-LAPNET great circle (e.g., events 2008-08-25T11:25:19.310 and 2008-11-21T07:05:34.940), no large P_{dmc} is present, indicating that P_{dmc} is unrelated to earthquakes.

Movie S1. Daily evolutions of winds, ocean wave heights, and secondary microseism source PSDs around New Zealand in 2008. The closed lines superposing the upper panels depict the contour values of 0.1, 0.5, and 0.9 for the weights shown in Fig. 5(c). The source PSDs are modulated by the bathymetric factors shown in Fig. 5(e). In the bottom panel, the time series for the P_{dmc} strength and the weighted averages of the source PSD, wave height, and wind speed in the effective source region, are the same as those in Fig. 6 in the main text. See captions of Figs 5 and 6 for more details.